Mass-Conserving Inversion of NO_x Emissions and Inferred Combustion Technologies in Energy Rich Northern China Based on Multi-Year Daily Remotely Sensed and Continuous Surface Measurements

Xiaolu Li[1,2], Jason Blake Cohen[2]*, Kai Qin[2*], Hong Geng[1], Liling Wu[3], Xiaohui Wu[4], Chengli Yang[4], Rui Zhang[5], Liqin Zhang[6]

[1]Institute of Environmental Science, Shanxi University, Taiyuan, China

[2]School of Environment and Spatial Informatics, China University of Mining and Technology, Xuzhou, China

[3]School of Environment, Tsinghua University, Beijing, China

[4]Shanxi Dadi Ecology and Environment Technology Research Institute Co., Ltd., Taiyuan, China

[5]Shanxi Institute of Eco-environmental Planning and Technology, Taiyuan, China

[6]Monitoring and Emergency Response Center of Ecology and Environment of Shanxi Province (Shanxi Institute of Ecologic and Environmental Science), Taiyuan, China

Corresponding authors: J. B. Cohen (jasonbc@alum.mit.edu), K. Qin (qinkai@cumt.edu.cn)

Key Points:

- Daily-scale, grid-by-grid emissions calculated using TROPOMI NO_2 and CEMS compare well with known spatial and temporal features
- Identification and quantification of different energy consuming combustion technologies based on the method's constrained NO_x/NO_2 ratio
- Variance maximization on TROPOMI NO_2 identifies and attributes variation to NO_x emissions, UVAI, and atmospheric transport of CO

Abstract

Nitrogen oxides (NO_x) are markers of combustion contributing to ozone, secondary aerosol, and acid rain, and are required to run models focusing on atmospheric environmental protection. This work presents a new model free inversion estimation framework using daily TROPOMI NO_2 columns and observed fluxes from the continuous emissions monitoring systems (CEMS) to quantify emissions of NO_x at 0.05°×0.05°. The average emission is 0.72±0.11Tg/yr from 2019 through 2021 over Shanxi, a major energy producing and consuming province in Northern China. The resulting emissions demonstrates significant spatial and temporal differences with bottom-up emissions databases, with 54% of the emissions concentrated in 25% of the total area. Two major forcing factors are horizontal advective transport (352.0±51.2km) and first order chemical loss (13.1±1.1hours), consistent with a non-insignificant amount of NO_x advected into the free troposphere. The third forcing factor, the computed ratio of NO_x/NO_2, on a pixel-by-pixel basis has a significant correlation with the combustion temperature and energy efficiency of large energy consuming sources. Specifically, thermal power plants, cement, and iron and steel companies have high NO_x/NO_2 ratios, while coking, industrial boilers, and aluminum show low ratios. Variance maximization applied to the daily TROPOMI NO_2 columns identifies three modes dominate the variance and attributes them to this work's computed emissions, remotely sensed TROPOMI UVAI, and transport based on TROPOMI CO. Using satellite observations for emission estimates in connection with CEMS allows the rapid update of emissions, while also providing scientific support for the identification and attribution of anthropogenic sources.

Plain Language Summary

Daily remotely sensed measurements of NO_2 from satellite and ground-based measurements of NO_x fluxes from industrial sources, in combination with a simplified mathematical method are used to estimate the emissions of NO_x. Sourcess are identified in regions previously not identified and quantified in regions which have been mis-identified or otherwise are missing up-to-date inventories. The underlying driving terms of this approach allow for flexible estimation of three driving factors: the thermodynamics of combustion and rapid atmospheric adjustment, first order chemical loss, and atmospheric transport. A deeper analysis with the thermodynamic term matches with different large energy consuming sources, being able to separate very hot sources such as power generation, iron, and cement from cooler or less energy efficient sources such as coking, industrial boilers, and aluminum smelting. The second and third terms are consistent with chemical and dynamical theory, and indicate that some of the emissions are lofted high above the surface. Analysis of the variance in the NO_2 columns identifies three major factors contributing to extremes: this work's emissions, measured UV radiation, and measurements of the gradient of measured CO. While the average emissions is not considerably different from existing datasets, the day-to-day and geospatial differences are significant.

1 Introduction

Economic growth has always been accompanied by air pollution, with serious consequences associated with higher atmospheric loadings. To alleviate severe air quality problems, the Chinese government has been implementing new air pollution controls, with the aim of producing higher-quality development. Two recent examples are the Air Pollution Prevention and Control Action Plan from 2013 to 2017 and the Three-Year Action Plan for Winning the Battle in Defense of Blue Sky from 2018 to 2020 (Geng et al., 2019; Jiang et al., 2021), which have led to a significant reduction in annual average concentrations of particulate

matter (PM), sulfur dioxide (SO_2) and carbon monoxide (CO) in Shanxi Province . Shanxi is selected for this study, as it is a highly energy rich location that produces more than 25% of all of China's coal, as well as having substantial industry that consumes a significant amount of the coal for both local energy production and export, steel, cement, coke, and aluminum production, among other economic activities (Li et al., 2022). Furthermore, due to its relatively dry climate, high elevation, and mountainous geography, it has complex underlying natural factors also impacting its atmospheric environment. For these reasons, there have also been minor increases in the annual average concentration of both ozone (O_3) and nitrogen dioxide (NO_2) observed in Shanxi between 2015 and 2020 (Shanxi DEE., 2016, 2021).

The sum of NO_2 and Nitrogen Monoxide (NO) is frequently grouped as nitrogen oxides (herein termed NO_x), which is an important trace gas impacting of the Earth's atmosphere because it is a strong marker of anthropogenic combustion-related pollution, a precursor to ozone (Jacob et al., 1993), secondary aerosol (Beirle et al., 2011) and acid rain (Singh & Agrawal, 2007). In order to gain a better understanding of NO_x and its impacts, precise and quantitative emissions inventories are crucial information for policy makers, air quality modelers, and anyone who works with chemical transport or chemical climate models, among others (Crippa et al., 2018; Hoesly et al., 2018). To improve the understanding of pollution and its environmental impacts, accurate quantitative knowledge of NO_x emissions at a very high horizontal resolution (e.g., 0.05°×0.05°) and daily temporal resolution is important, but tends to be either lacking and/or increasingly uncertain (Kong et al., 2019; Zheng et al., 2017).

Presently, most emission inventories are compiled from statistics on emitting activities and associated typical emission factors, herein called "Bottom Up" approaches, which are subject to substantial uncertainties. On-site surveys are time consuming and resource demanding, and therefore difficult to be applied to a large domain in a timely manner (Mijling & van der A, 2012; Zhao et al., 2011). Differences between small field studies and controlled laboratory combustion experiments and real-world examples also are quite significant, with super-emitters known to create large differences when using insufficiently large datasets (Zavala et al., 2006). With low temporal resolution these bottom-up inventories are not able to keep up with rapid changes in industries and economic activities, and therefore are not very good at tracking atmospheric emissions under actual existing environmental conditions, limiting their use (Mijling & van der A, 2012).

Attempts at top-down emissions inventories have been made by the community, with most focusing on applications to long-lived gasses (CH_4, CFCs, and N_2O), since their chemical decay is very slow compared with their transport processes, allowing for much simpler set of equations required to perform the inversion (Chen & Prinn, 2006; Tu, Hase, et al., 2022). Only a very small number of past works have focused on top-down emissions estimation of short-lived species, and the few that have always do so under a set of idealized conditions. Some limit their investigations to where there is a strong single point source surrounded by what is otherwise relatively clean (Lin et al., 2020), others use an underlying model to approximate chemical and transport properties of the short lived species over a pseudo region which is climatologically similar, and others use highly complex or overfitting approaches such as data assimilation and Kalman filters which work very well but are susceptible to underlying model and scientific uncertainty, as well as being extremely costly to run (Cohen & Wang, 2014; Zhang et al., 2021;Hu et al., 2022). Others have attempted to use satellite observations to scale existing top-down emissions inventories, to make spatially consistent, high spatial resolution maps, but have

a hard time being applied in regions where the a priori emission is zero (Liu & Cohen, 2022; Wang et al., 2021).

This study takes advantage of the respective strengths of top-down and bottom-up emissions estimation by applying a new, fast, first-order approach based on daily measurements of remotely sensed NO_2 from the Tropospheric Monitoring Instrument (TROPOMI), winds, and mass conserving estimates of in-situ chemical and physical processing to estimate the daily NO_x emissions on a mesoscale grid at (0.05°×0.05°) from 2019 through 2021. This work relies on the continuous emissions monitoring systems (CEMS) measurements from significant combustion sources as the source of a priori emission information. This net combination of factors does not rely on complex models, and allows a flexible approximation of the first order driving forces of thermodynamics, chemistry, and transport. This unique perspective is capable of inverting emissions using different driving forces under different but realistic environmental conditions, including during different months of the year, over multi-year changes in the environment, under high UV and low UV conditions, under complex meteorological domains, and over sources which are both thermodynamically stable as well as unstable. Finally, this approach allows a robust error quantification, and compares very well with the measured spatial and temporal variation in the underlying remotely sensed NO_2 columns.

2 Materials and Methods

2.1 Tropospheric Vertical Column Measurements from TROPOMI

TROPOMI measures reflected solar radiation in the UV, visible, and Near IR bands following a sun-synchronous, low-earth orbit with an equator overpass time of approximately 13:30 local solar time, allowing daily-scale measurements across the globe(Goldberg et al., 2019; Tu, Schneider, et al., 2022; Veefkind et al., 2012). Starting from August 2019, the spatial resolution of TROPOMI has been refined to 5.5km×3.5km (Lange et al., 2022). This study specifically uses three distinct products measured by TROPOMI over different radiative bands, but at the same place and time: NO_2, CO, and UVAI.

This work specifically uses daily level-2 version 2.3.1 tropospheric NO_2 columns, daily level-2 version 2.2.0 CO columns, and daily level-2 version 2.2.0 UVAI over Shanxi Province. All available days and swaths corresponding to the time period from 1 January 2019 through 14 November 2021 are analyzed (https://disc.gsfc.nasa.gov/datasets). Overlapping NO_2, CO, and UVAI column pixels in each swath are resampled to a common latitude-longitude grid at 0.05°×0.05° using weighted polygons (http://stcorp.github.io/harp/doc/html/index.html). Before use, it is require that all TROPOMI data is quality assured, specifically insisting that each pixel has a "qa_value" greater than 0.75, that the "cloud radiance fraction" is smaller than 0.5, and that scenes covered by snow/ice, errors and similar problematic retrievals are removed (Eskes, H., 2021). Furthermore, in the case of NO_2, an additional filter is applied to avoid issues where the signal is possibly smaller than the uncertainty range of 1.0×10^{15}+30% molec/cm^2 (Qin et al., 2022), leading to all grids with a column loading smaller than 1.4×10^{15}molec/cm^2 being discarded. This combination of assumptions ensures that the data used should be of higher precision than the a priori emissions datasets used later in this work.

The TROPOMI NO_2 columns used in this study can portray the spatial and temporal distribution of sources in a high amount of detail, including being able to effectively identify spatial hotspots (Griffin et al., 2019). The climatological mean and standard deviation of these

columns are shown in Figure 1, and are consistent with surface measurements indicating that the most polluted areas with respect to NO_2 in Shanxi are mainly concentrated in Fen River valley bottom area, containing Taiyuan Basin, Xinding Basin, Linfen Basin, and Yangquan City. Areas with a high standard deviation and relatively low mean value are observed in regions where new economic development zones containing power plants, coke enterprises and some other raw materials producing factories have been established, as observed in Datong. Areas with a relatively high standard deviation and relatively high mean value are indicative of high urbanization, and correspond consistently with the Taiyuan Basin, Xinding Basin, and southern Yangquan. Areas with a high average value and a low standard deviation correspond with areas which have a fewer number of temporally consistent emissions sources, as is observed in some high altitude areas, and small parts of the Linfen Basin, central Changzhi, Lvliang and Jincheng.

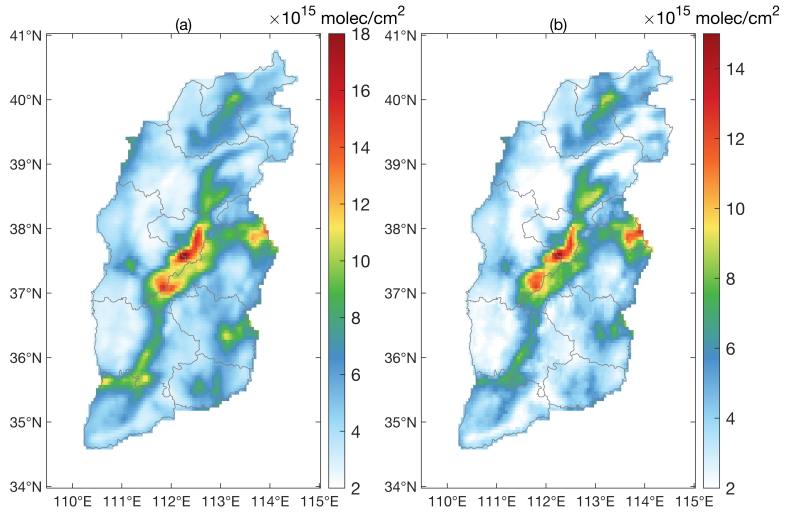

Figure 1. Climatology of TROPOMI daily NO_2 column loadings from 2019 through 2021: (a) mean, and (b) standard deviation.

2.2 A Prior Emissions inventories

2.2.1 CEMS

CEMS was introduced by the Ministry of Environmental Protection of China in 2007 to monitor and manage the emissions of certain (mainly high-emitting) plants (Karplus et al., 2018; Schreifels et al., 2012). These systems make actual measurements of stack concentration PM, SO_2 and NO_x, as discharged from coal power plants, steel and iron plants, aluminum smelters, coke plants, coal-fired boilers and others, all in real-time (Tang et al., 2020; Zhang & Schreifels, 2011). Statistics of the emissions sites monitored in Shanxi are given in Table1 and displayed in Figure 2. The NO_x concentration was measured in two different ways: one converts NO_2 to NO and measures the NO concentration uniformly, the other measures both NO_2 and NO, and converts the total amount into an NO_2 mass concentration. Unfortunately, the results are not labeled as to which device was used at each individual stack, and therefore some error is introduced.

In this work, all available CEMS monitors of daily-scale emissions from 2019 to 2021 were obtained from the Department of Ecology and Environment of Shanxi Province (original data from the government repository located at https://sthjt.shanxi.gov.cn/wryjg/, and available in English at https://figshare.com/s/22782c33cbc4e61afd25), with the government making great effort to regulate the CEMS network and to ensure the reliability of CEMS data (Tang et al., 2020). Before using the data, preprocessing includes using google earth to correct the location of the factories, removing all null observations, and setting abnormal values (including zero or negative fluxes, and abnormally large fluxes) to NaN. The overall percentage of abnormal values is found to account for 0.14%, 0.09%, and 0.18% of the raw data respectively for 2019, 2020 and 2021. The formula used to calculate NO_x emissions is given in eqution (1)

$$E_d = \overline{C_h} \times \overline{Q_h} \times 24 \quad (1)$$

where $\overline{C_h}$ is the daily average of hourly NO_x concentration and $\overline{Q_h}$ is the daily average of hourly wet flue gas flow under actual working conditions following procedure HJ76-2017 (Zhang & Schreifels, 2011). The uncertainty of NO_x concentration (C_h) when $C_h \geq 513 mg/m^3$ is 85%, when $103 mg/m^3 \leq C_h < 513 mg/m^3$ is ±41mg/m, when $41 mg/m^3 \leq C_h < 103 mg/m^3$ is ±30%, and when $C_h < 41 mg/m^3$ is $\pm 12 mg/m^3$. After quality control, the emission intensity on a grid-by-grid basis is found to be 0.54±0.40μg/m^2•s, 0.34±0.26μg/m^2•s, and 0.39±0.24 μg/m^2•s for 2019, 2020 and 2021, respectively. Grid-by-grid 3-year climatological emissions, and PDFs of annual grid-by-grid average emissions are given in Figure 2.

Table 1. Summary statistics for plants included in CEMS.

Year	Number of Companies	Number of Stacks monitored	Missing days (d)	Percentage of missing days (%)
2019	470	1557	102	27.9
2020	542	2187	24	6.6
2021	513	1806	0	0

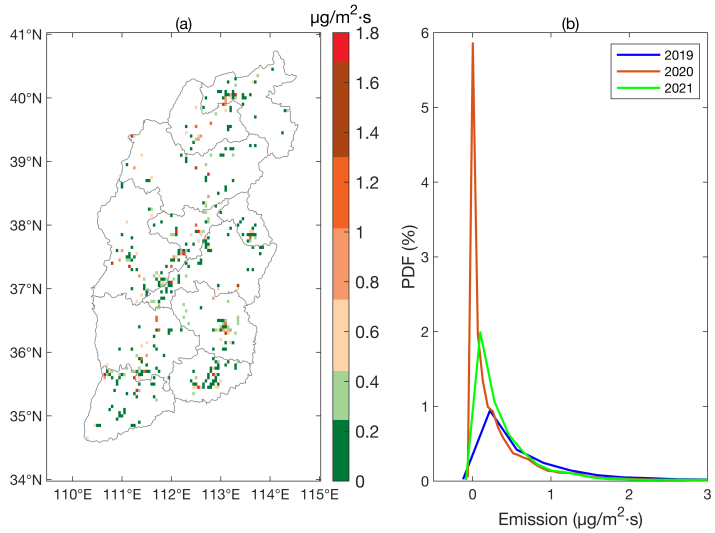

Figure 2: Climatology of daily CEMS emissions data from 2019 through 2021: (a) 3-year average gridded NO_x Emissions, and (b) PDFs of day-by-day and grid-by-grid Emissions over individual years.

2.2.2 Multi-resolution Emission Inventory for China (MEIC)

MEIC provides 0.25°×0.25° bottom-up emissions of anthropogenic air pollutants over mainland China, with monthly NO_x emissions provided for the agriculture, industry, power, residential and transportation sectors. This work uses data from 2019 and 2020 (Zheng et al., 2021). To match with the higher resolution TROPOMI grids, the MEIC data is mapped to the TROPOMI 0.05°×0.05° grid, with each grid assigned the same flux as the underlying MEIC grid. To ensure quality control, given that many very low values may fall within the uncertainty of the bottom-up emissions process (Bond, 2004; J. B. Cohen & Wang, 2014; Crippa et al., 2018) different minimum cutoffs have been applied to the MEIC data prior to use as an a priori, which herein are labeled as MEIC014 (discarding all values smaller than 0.14 μg/m^2·s) and MEIC050 (discarding all values smaller than 0.50 μg/m^2·s). MEIC014 discards 69% and 71% percent of the grids respectively in 2019 and 2020, while MEIC050 discards 91% and 92% grids respectively. The mean daily values and PDFs of the grid-by-grid climatological mean data over Shanxi Province from 2019 January 1 to 2020 December 31 are given in Figure 3(a) and Figure 3 (b).

2.2.3 Merged MEIC and CEMS Emissions

The already processed CEMS and MEIC emissions which occur on the same grid at the same time are fused into a new joint product. This new product [hereafter called Merged Emissions] contains MEIC with power plant and industrial emissions removed, summed together with the CEMS data. This is done on a day-to-day basis from January 2019 through December 2020. Since there are many very small values in the merged inventory which are not realistic, all grids with data lower than 0.14 μg/m^2·s, 91% and 92% of grids respectively in 2019 and 2020, are excluded in a second merged product [hereafter called Merged014]. The climatological mean

of daily emissions, and histograms of day-by-day and grid-by-grid values over Shanxi are given in Figure 3(c) and Figure 3 (d).

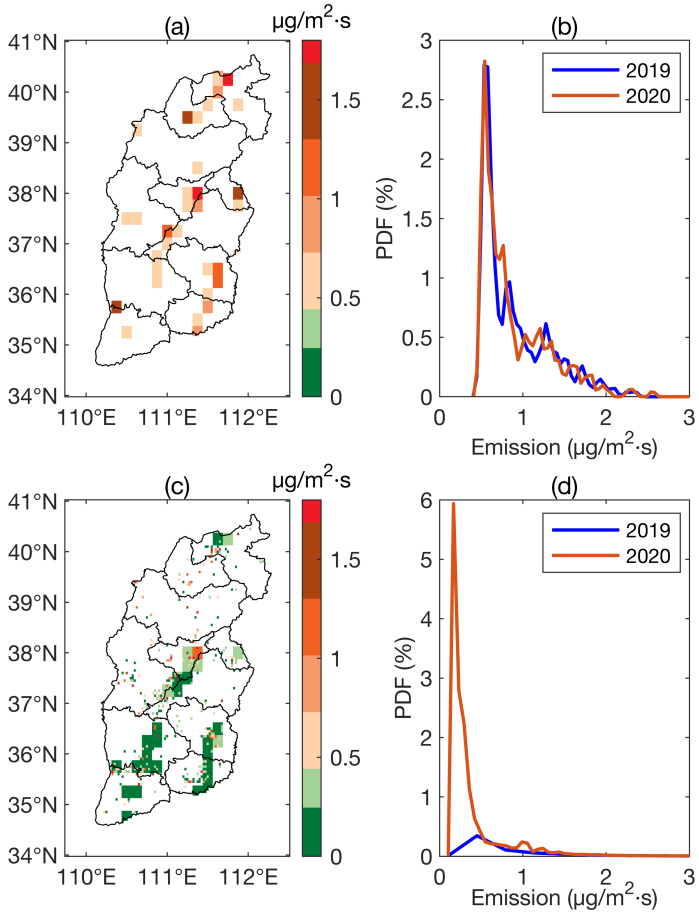

Figure 3: Daily average MEIC and Merged emissions from 2019 to 2020: (a) Climatological mean of MEIC050; (b) histograms of day-by-day and grid-by-grid MEIC050 over individual years; (c) Climatological mean of Merged014; (d) histograms of day-by-day and grid-by-grid Merged014 over individual years.

2.3 Wind

Wind speed and direction are from the European Centre for Medium-Range Weather Forecasts, ERA-5 reanalysis product. In specific, we use 6-hourly 6AM UTC u and v wind products (closest in terms of time to the TROPOMI overpass) at 900mb and 0.25°×0.25° resolution (Lange et al., 2022), available at https://www.ecmwf.int/en/forecasts/dataset/ecmwf-reanalysis-v5. To merge the wind data in space and time with the TROPOMI observations, they are linearly interpolated to the center of each TROPOMI 0.05°×0.05° grid (Fioletov et al., 2022). The reason for choosing the 900mb level is two-fold. First, Shanxi has complex topography, leading to a significant amount of pollutant transport from near the ground to the lower free troposphere. Second, due to the relatively dry conditions, vertical plume-based rise is thought to not be insignificant (Wang et al., 2020). Overall, this height is a reasonable approximation of the

corresponding median height of the expected total NOx emissions and median of the wind speed and directions (Lange et al., 2022).

2.4 Variance Maximization

To extract the spatial and temporal features of the extremes of the remotely sensed NO_2 fields in an unbiased manner, the empirical orthogonal functions method is applied. This technique decomposes the data into a set of orthogonal standing signals in space [EOF] and in time, with those signals contributing the most to the overall variance of the underlying dataset, representing unique phenomenon that control the overall characteristics of the NO_2 columns (Lin et al., 2020; Zhou et al., 2016). Further details including mathematical derivations are given in (Björnsson & Venegas, 1997) and (Cohen, 2014). This work retains the first three EOFs, which are found to contribute to 29.7%, 8.5%, and 4.2% of the total variation, with the subsequent EOFs each contributing an insignificant amount and therefore no longer considered in this work.

2.5 Model Free Inversion Estimation Framework

In the case where there is an observed change in the stock of NO_x in the atmosphere, herein represented as S, this can only be accomplished by introducing some sources or sinks. The first is the amount of NO_x emitted, herein represented as E, which always will increase the existing stock. The second is chemical loss of NO_x, which will always lead to a decrease in the existing stock. The third is the sum of pressure induced and advective transport, which may either increase or decrease the stock. The chemical sinks of NO_x are dominated by the reaction between NO_2 with OH (Beirle et al., 2019; Valin et al., 2013), which can be described as C. The transport is herein described as D, and is calculated by the gradient of the multiple of the u and v wind fields times the top-down NO_x column loadings, herein described as V_{NOx} , which consists of an advective portion (H. Wang et al., 2014) and a pressure-based portion (Mahowald et al., 2005). Hence, a simple mass conservation equation for NO_x loading can be calculated as

$$dS = E - C + D \tag{2}$$

Solving equation 2 for emissions on a grid-by-grid basis requires knowledge of the mass change of the loading in time, and detailed consideration of chemical loss and transformation, deposition, and transport. An explicit formulation of these processes into a readily solvable mass balance method is derived as equation 3. However, due to the fact that TROPOMI only measures NO_2 and not NO_x, a transformation is required to transform NO_2 columns into NO_x ($NO_x = \alpha_1 \cdot NO_2$). These details allow transformation of the mass balance equation into equation 4, where

$$E_{NOx} = \frac{dV_{NOx}}{dt} + \alpha \cdot V_{NOx} + \alpha' \cdot \nabla(\bar{u} \cdot V_{NO_x}) \tag{3}$$

$$E_{NOx} = \alpha_1 \cdot \frac{dV_{NO_2}}{dt} + \alpha_1\alpha_2 \cdot V_{NO_2} + \alpha_1\alpha_3 \cdot (\nabla(u \cdot V_{NO_2}) + \nabla(v \cdot V_{NO_2})) \tag{4}$$

α_2, α_3 are the parameters related to NO_x lifetime and transport distance, respectively.

2.6 Additional Analytical Methods

This work employs multiple linear regression to fit the values of α_1, α_2, and $\alpha_3$on a month-by-month, grid-by-grid basis using all available daily measurements and equation 4. Bootstrapping is a means to create a new sample to represent the parent sample distribution through multiple repetitions of sampling(Liu & Cohen, 2022). In specific, the distributions of α_1,

α_2, and α_3 are sampled across the central 90% of their probability distributions, to use to generate a set of pseudo α_1, α_2, and α_3 on individual grids where there is no existing a priori and therefore no actual solution of these variables. These bootstrapped pseudo α_1, α_2, and α_3 are then used on these specific grids to approximate the emissions of NO_x using equation 4 on a daily basis where TROPOMI NO_2 column data and wind data is available.

3 Results and Discussion

3.1 Computed Emissions and Fitting Parameters Using CEMS

First, the CEMS a priori emissions dataset is used together with TROPOMI NO_2 column loadings, wind, and equation 4 to fit the values of α_1, α_2, and α_3, as given in section 2.6. The fitted coefficients are computed month-by-month over the three years of data. Their overall climatological mean and standard deviation are found to be α_1=6.1±1.3, α_2=13.1±1.1h, and α_3=352.0±51.2km. However, it is observed in the fits that there is some variability which is not uniform in space and time, with the month-by-month values and standard deviations given in Figure 4. In general, α_1 tends to be slightly higher during the hotter months of the year, but it also has a higher variability when the UV values are high as well, making July and August the only months in which it statistically has fewer small values than the other times of the year. In general, α_2 tends to be quite variable, without any significant seasonal or month of year pattern. Instead, both inter-annual and intra-annual variations seem to drive most of the change. Given that this is related to the overall average temperature and UV availability, a complex function of the plume height, cloudiness, aerosol loadings, and other factors, this is not unreasonable. The absolute magnitudes of α_2 and their uncertainty range are reasonable when compared with vertically integrated and 24-hour integrated chemical transport model values. In general, α_3 also seems to not have any significant seasonal or monthly pattern, with inter-annual and intra-annual terms seeming to dominate. The values tend to be slightly larger than chemical transport models account for, but are reasonable when compared with the ultra-long-range transport simulated for plumes which break the boundary layer. This range, combined with the wide mountain basins in Shanxi of 200km to 300km in length, seem to provide a reasonable bound on the output results.

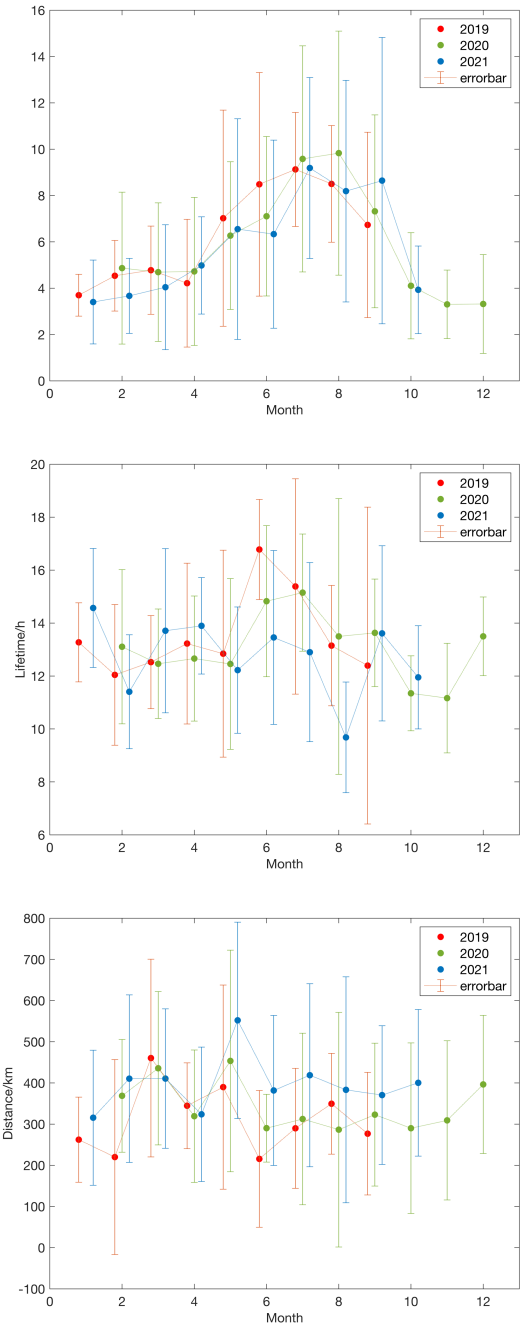

Figure 4: Monthly α_1 (top), α_2 (middle) and α_3 (bottom) calculated based on CEMS. Data from different years is provided where 2019 is in red, 2020 is in green, and 2021 is in blue.

Next, the daily emissions of NO_x are calculated throughout the given spatial and temporal domain of interest using bootstrapping in connection with equation 4 and the fitted values of α_1, α_2, and α_3. The use of the Model Free Inversion Estimation Framework [MFIEF] can effectively optimize the distribution of the inventory and perform inventory correction based on satellite

data, while complementing many areas where there is no existing emissions data, incomplete data, mis-characterized data, or data which may be reasonable on average but not account for daily-scale variability. The day-to-day, grid-by-grid emissions are displayed in terms of climatology, day-to-day variability, and average mean error based on the standard deviation of the bootstrap, in Figure 5. For all subsequent emissions values displayed, the numbers correspond to the sum over the daily mean ± daily variation. It is observed that the grids with the highest NO_x emission in Shanxi are mainly concentrated in the lower Fen River valley, containing the Taiyuan Basin, the Xinding Basin, and the LinFen Basin, which also corresponds to the area containing the highest population density in the region studied. This area in total accounts for 25% of the total area of the province and contributes 54% (0.39±0.059 Tg NO_x/yr) of the total (0.72±0.11 Tg NO_x/yr) in Shanxi. It is of significance to note that regions with a grid-by-grid moderate amount of emissions, ranging from 0.5 to 1.5 $\mu g/m^2 \cdot s$, contribute a of 38% of the emissions (0.36±0.13 Tg NO_x/yr).

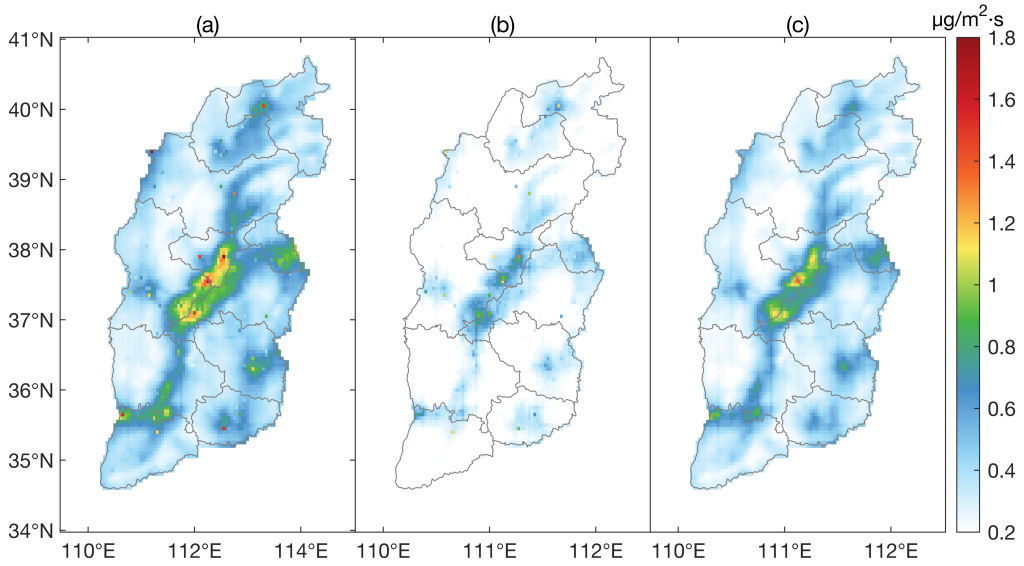

Figure 5: Daily emissions based on CEMS from Jan 2019 to Oct 2020 over Shanxi Province at 0.05° × 0.05°: (a) Climatological mean of NO_x emissions. (b) Climatological standard deviation of NO_x emissions (day-to-day variability). (c) Bootstrapping standard deviation (uncertainty).

3.2 Underlying Factors Contributing to Variance Maximized TROPOMI NO_2 Columns

A deeper analysis of the factors contributing to the variance in the TROPOMI NO_2 column measurements is essential to determine if the computed emissions and underlying factors are consistent with the remotely sensed fields both in terms of grid-by-grid mean value and temporal variability. Recent best practice has devised a way to ensure this consistency through the use of an Empirical Orthogonal Functions Principal Components Analysis (Cohen, 2014; Cohen et al., 2017; Lin et al., 2020), which is applied to the daily TROPOMI NO_2 columns. The three spatial modes contributing the most variation to the observed daily TROPOMI NO_2 fields [EOF1, EOF2, and EOF3] contribute 29.7%, 8.5%, and 4.2% respectively, as shown in Figure 6.

It is asserted that EOF1 is directly driven by the CEMS computed NO_x emissions. The comparison of EOF1 and the emissions is shown in Figure 7. By applying 4 different

progressively increasing cutoffs to the domain of EOF1, it is observed that as the EOF1 domain increases in magnitude, that the 3-year mean NOx emissions computed over the same domains also increase in magnitude. Therefore, the more extreme the EOF1 value, the higher the emissions, demonstrating that the emissions are responsible for the first mode of the maximized variance.

Second, it is asserted that EOF2 is related to measured UV radiation, providing measurement support of the theory in which UV radiation plays a role driving the chemical decay of NO_x. Applying 4 different cutoffs to EOF2, it is observed that as the EOF2 domain increase in magnitude, that the 3-year mean measured TROPOMI UVAI decreases, as demonstrated in Figure 8. Since UVAI scales inversely with the available surface UV radiation, therefore lower UVAI implies higher available surface UV radiation, and implicitly faster chemical decay of NO_x. This result demonstrates that surface UV radiation is responsible for the second mode of the maximized variance.

Finally, it is asserted that EOF3 is related to the transport of CO, which makes sense in that CO can undergo transport over longer distances than NO_x due to its slower chemical decay, and therefore represents the long-range transport of not only itself but also many other chemical species into the local environment being analyzed. This term has been specifically computed by taking the variance of the multiple of wind and TROPOMI measured CO column loadings, specifically $\nabla(\bar{u} \cdot V_{CO})$. Similarly to the above cases, it is demonstrated that as 4 different cutoffs are applied to EOF3, it is observed that as the EOF3 domain increase in magnitude, so does the measured long-range transport based on TROPOMI CO also increase, as observed in Figure 9. Therefore, long-range transport is responsible for the third mode of the maximized variance.

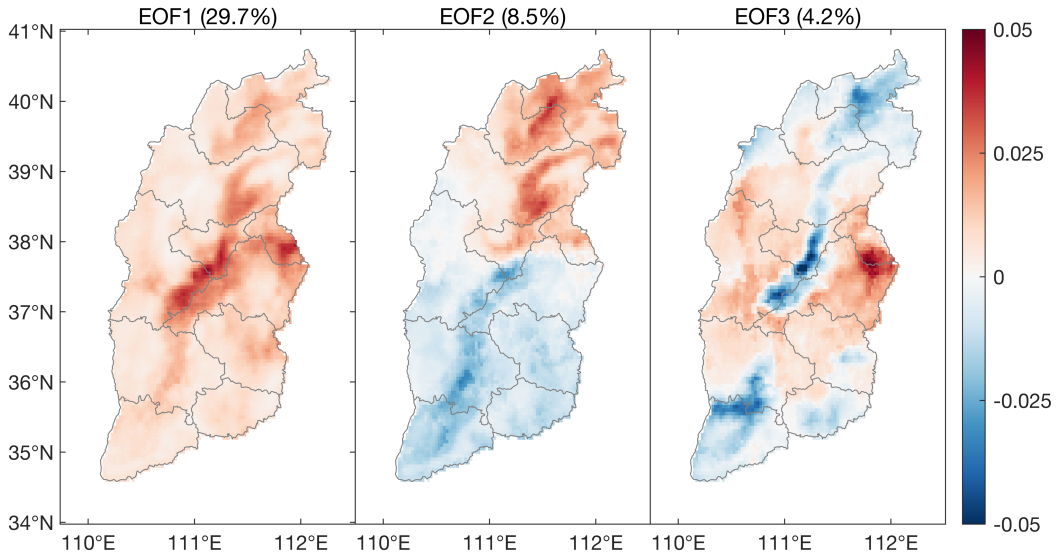

Figure 6: Spatial distribution map of (a) EOF1, (b) EOF2, and (c) EOF3.

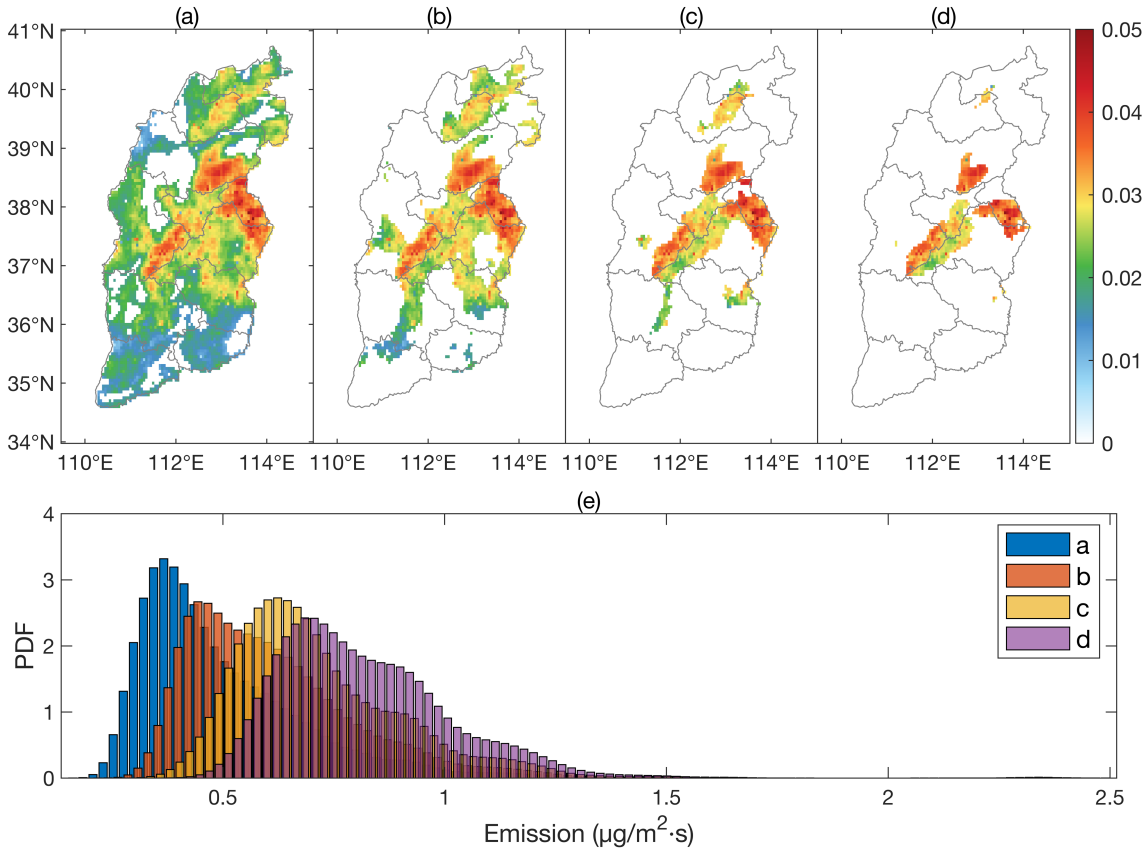

384

385 **Figure 7:** Four different cutoffs of EOF1 are used to set the domains. The maps in (a-d) are plots
386 of EOF1/Emissions where the cutoffs are given as (a) EOF1 >0.005, (b) EOF1 >0.01, (c)
387 EOF1 >0.015, (d) EOF1 >0.02. (e) Histograms of the emissions over the domains given
388 respectively in a-d.

389

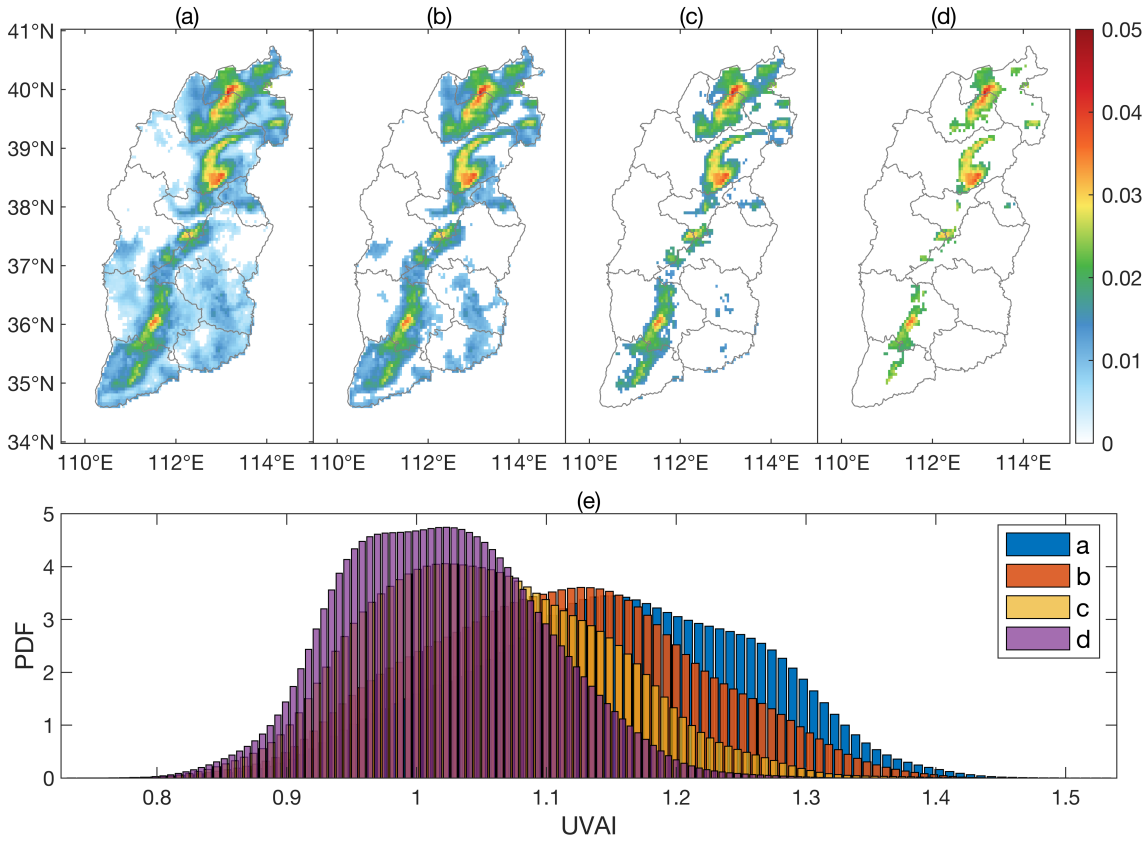

Figure 8: Four different cutoffs of EOF2 are used to set the domains. The maps in (a-d) are plots of EOF2/UVAI where the cutoffs are given as (a) EOF2 >0.005, (b) EOF2 >0.01, (c) EOF2 >0.015, (d) EOF2 >0.02. (e) Histograms of the UVAI over the domains given respectively in a-d.

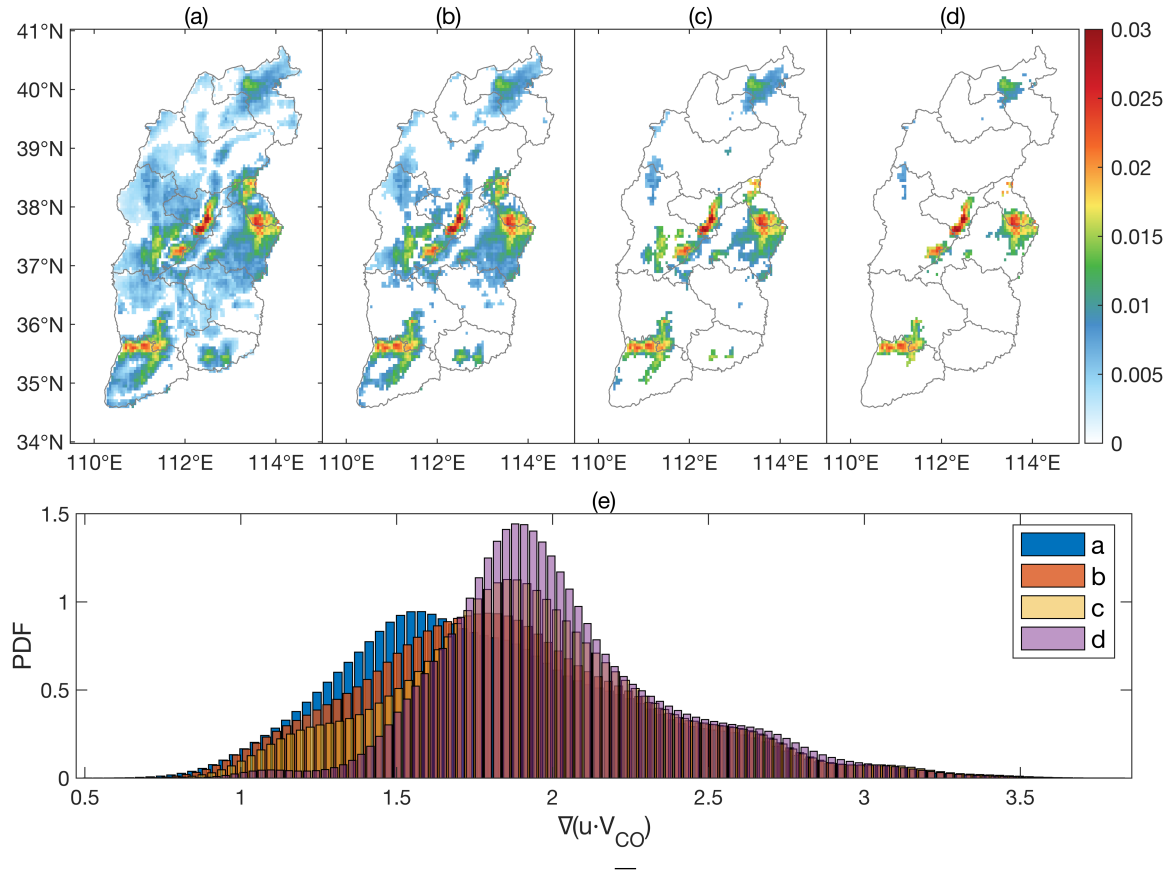

Figure 9: Four different cutoffs of EOF3 are used to set the domains. The maps in (a-d) are plots of EOF1/CO-transport where the cutoffs are given as (a) EOF3 >0.005, (b) EOF3 >0.01, (c) EOF3 >0.015, (d) EOF3 >0.02. (e) Histograms of the CO-transport over the domains given respectively in a-d.

3.3 Application of α_1 to Analyze Different Combustion Technologies

A significant finding is observed when the value of α_1 is analyzed more closely on a pixel-by-pixel level and compared with underlying CEMS combustion source type. This analysis is motivated by the fact that NO_x is produced during high temperature combustion of air, with three different major parts contributing to the overall amount of NO_x produced: thermal NO_x formation, fuel NO_x formation and chemical NO_x formation (Le Bris et al., 2007; Schwerdt, 2006). This work demonstrates clearly that the values of α_1 are significantly related to the underlying thermodynamic conditions occurring at the time of combustion, allowing for many future applications of the results herein to better understand and monitor such plants around the world.

Thermal NO_x formation describes the process when N_2 in the air reacts with O_2 in the air at high temperatures (Le Bris et al., 2007), with NO_2 forming preferentially at temperatures between 800°C and 1200°C and NO forming preferentially at temperatures above 1200°C. Thermal NO_x usually dominates the overall NO_x emissions when the temperature is over 1100°C, and reaches a maximum contribution when the temperature is over 1600 °C. There is additional NO_x produced due to free nitrogen in the fuel itself. Finally, chemical decay may

occur when there are mixed organo-nitrides, resulting in the prompt NO_x formation. Therefore, a deeper understanding of the overall and oxygen partial pressures and temperature in the combustion chamber are all important for NO_x formation. First, as the temperature increases, the amount of NO produced will increase along with NO_2. When the temperature exceeds 1200℃, NO will continue to increase while NO_2 will decrease. Furthermore, when the pressure increases, the yield of NO_2 will also decrease and NO will increase (Aho et al., 1995; Turns, 1995).

In addition, in-situ processes also impact the value of α_1 since there is a rapid adjustment after emitted from a combustion stack into the atmosphere, before the parcel comes to thermodynamic equilibrium (Cohen et al., 2018; Wang et al., 2020). Figure 10 shows the results of α_1 calculated based on CEMS in this study, and it can be seen that the values are highest in the hottest months without maximum UV (July and August) and are lowest in the coldest months with the minimum UV (November, December, and January), with both factors moderating the combustion values during the atmospheric in-situ processing time. This is especially important in the case of hotter power sources, since they will contain more buoyancy, and rise to a higher height, making them more likely to be in contact with air which is more exposed to UV and also generally colder than the surface. Overall, the value of α_1 seems to rely on both the temperature under which the initial NO_x was generated, as well as any rapid processes taking place once it is emitted into the atmosphere (including chemistry and vertical lofting).

A deeper look at the various different CEMS plant sources reveals that the internal combustion processes are extremely important in terms of the overall value of α_1. Production of cement is a major source of NO_x in Shanxi, with the major technology being dry process rotary kiln technology. Given that the temperature of the main burner of cement rotary kilns are higher than 1400℃, with some peaking as high as 1800 ℃ to 2000 ℃ (Akgun, 2003; Wu et al., 2020), it is expected that there will be a large amount of thermodynamic NO_x generation. As observed at the cement CEMS sites, the computed α_1 has a value always within or above the error range of the values computed at powerplants, including some of the individually highest values, as show in figure 10b.

Steel and iron are produced through a set of different processes, involving combustion at a range of different temperatures. The steps involved in the blast furnaces as well as some other processes, require a high flame temperature, in the range from 1350 ℃ to 2000 ℃. There are further processes occurring that require a relatively lower temperature, such as in the sinter bed stage, where the highest temperature is only about 1300 ℃ (Zhou et al., 2018). Therefore, while in general the values are relatively high, and are usually found within the ranges of power plants, there are some individual values of α_1 computed which are slightly outside the range of the powerplant α_1 values, on both the high and low sides, as observed in figure 10c.

The maximum temperature of the combustion chamber of thermal power plants can reach 2000℃. In fact, many such plants are constantly finding ways to increase the combustion efficiency of power plants, so that they can be more energy efficient and produce as much energy per ton of CO_2 emitted, which in turn increases the combustion temperature. As observed in Figure10a, α_1 is relatively high at these sites, consistent with thermal production.

Industrial boilers use a similar technology as power plants, but tend to be smaller and run at a lower temperature range and efficiency. This is because their use is to produce hot water and steam for direct residential and industrial use, not high-pressure steam to run turbines. In general, these boilers have a much smaller overall capacity (as small as one tenth the total power output)

and therefore without access to CEMS, may not be otherwise be detectable. However, analyzing the values of α_1 over these sites corresponding to the CEMS map, as displayed in figure 10f, the results are found to have a value of α_1 that is lower than power plants in general, although also smooth and consistent over different months of the year. That these sites produce NO_x with a far greater amount of NO_2 than the above cases is as expected.

Coke and aluminum oxide are both produced using a different technique from the other combustion sources, specifically focusing on creating high temperature, oven-like conditions to bake/roast their products. The average temperature of the coke oven charring chamber and aluminum oxide roasting furnace are around 1000°C (Neto et al., 2021; Abyzov, 2019), with the material temperature continuously held in that temperature for a long period of time, e.g., one day. At the same time, the oxygen content is low. Aluminum is also smelted in an oven-like condition. In net, there is far less thermal NO and more thermal NO_2. Correspondingly, the values of α_1 are relatively lower, as detailed in figure 10d and figure 10e. Furthermore, due to very different technologies and input materials used, the results are also observed to have a far greater variance both intra-annually and inter-annually than the other sources.

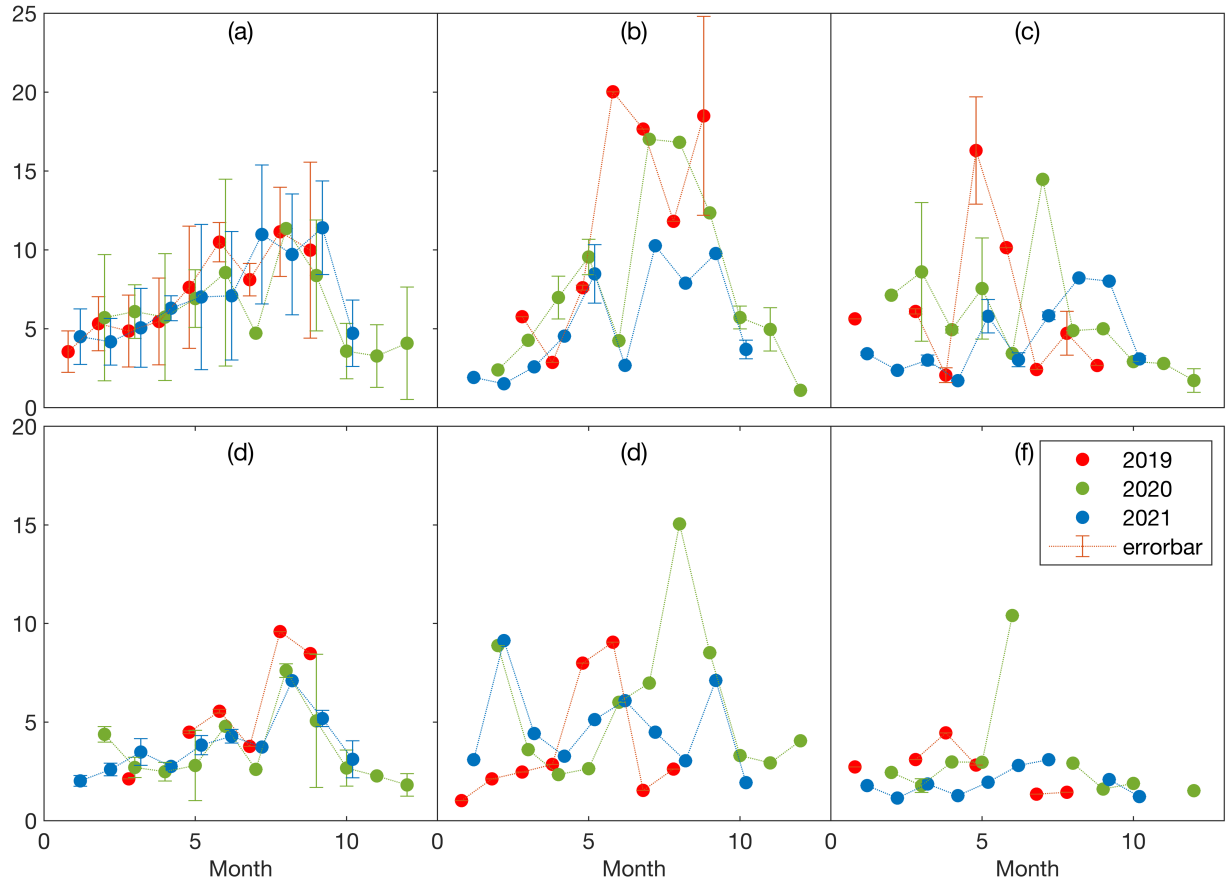

Figure 10: Monthly α_1 calculated based on CEMS for different factories of 2019, 2020 and 2021, respectively: (top-left) Power plants; (top-center) Cement factories; (top-right) Steel and iron factories; (bottom-left) Coke ovens; (bottom-center) Aluminum oxide factories; (bottom-right) Boilers.

3.4 Yearly Changes of CEMS Calculated Emissions

Figure 11 shows the calculated results of CEMS emissions from February to September in 2019, 2020, and 2021, have average emission intensities of 0.52±0.31, 0.42±0.21, and 0.37±0.18 μg/m^2•s, respectively. The emission intensity in 2020 is much less than that in 2019, with a continued albeit smaller decrease from 2020 to 2021, coupled with a continued reduction in the day-to-day variability. This overall change is because of the more stagnant production and other related economic activities during the control of COVID-19 in 2020, as well as a strong overlap with long-term air pollution control measurements, such as the ultra-low strategy on steel and iron, and cement factories, which were put in place long before COVID-19 and expected to successfully achieve a low emissions level by the end of 2021.

There are also some differences in hotspot areas. By comparing with the distribution map of industrial parks, CEMS enterprises, and district and county distribution map in Shanxi, it can be found that almost all of the individual grids with an increase in emissions in 2020 occur in areas outside industrial and city center areas. In specific, the most obvious increase is observed

in the rural boarder area between southeastern Shanxi and Henan Province, including parts of Lingchuan, Gaoping, Zezhou, and Qinshui Counties and areas outside of the urban area of Jincheng City. Huguan, Pinshun, Licheng Counties in Changzhi City, Zuoquan and Heshun Counties in Jinzhong City adjacent to Handan City in Hebei Province also have a large increase. While a part of this increase may be due to transport from surrounding areas of adjacent provinces, based on the results of Figure 9 this is not very significant. Therefore, the most likely explanation is that when COVID-19 first occurred, people stayed in their rural hometowns and continued to cook and heat their homes, as compared to moving to the urban areas for employment. Similarly, the reduction in emissions in urban and industrial areas is mainly due to the reduction in industrial production and of shrinking transport flow in cities. Part of the increase in 2021 relative to 2020 is observed in grids where there is an observed resumption of previously shutdown industries and the widespread resumption of road traffic. Jincheng, Changzhi, and Jinzhong Cities increased obviously in 2020 but then saturated and did not show a significant increase during 2021. The southwest corner of Shanxi, Linfen, Yuncheng Cities and other places increased more in 2021, perhaps related to increased production and subsequent pollution transport from Henan and Shaanxi Provinces, as consistent with Figure 12b. From the two-year change (figure 12c), the overall emissions of NO_x demonstrate a very obvious weakening, especially in Datong, the Xinding basin, and the Taiyuan basin, which includes the largest city centers and industrial belts in the province.

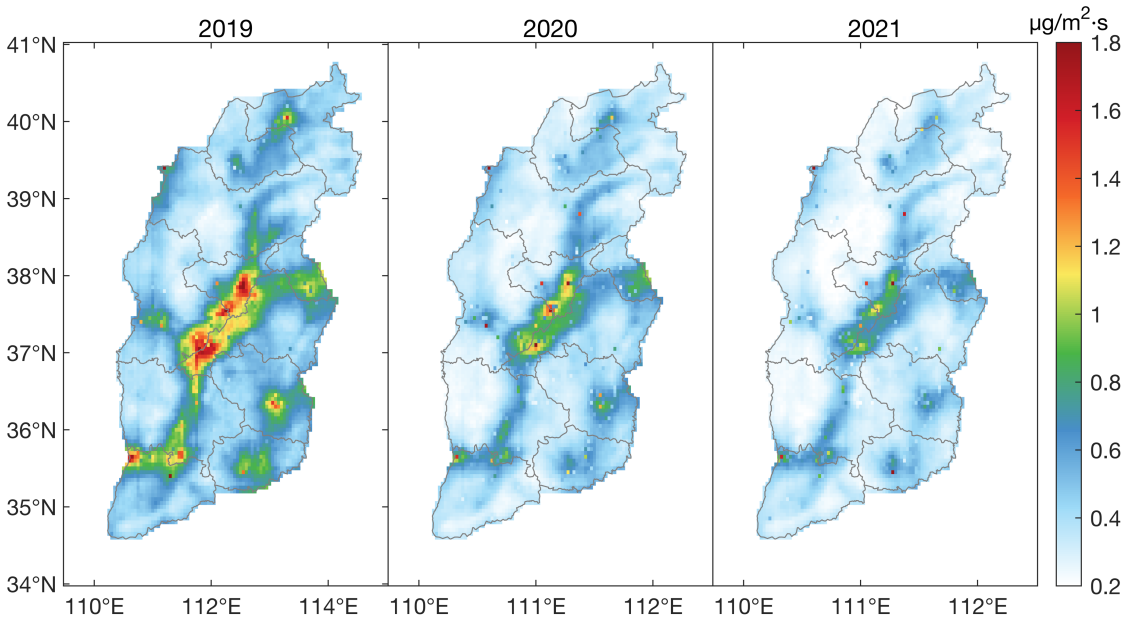

515

516 **Figure 11:** Daily average NOx emissions based on CEMS in different years: (a) Climatological
517 mean emissions of 2019 February to September; (b) Climatological mean of 2020 February to
518 September; (c) Climatological mean of 2021 February to September.

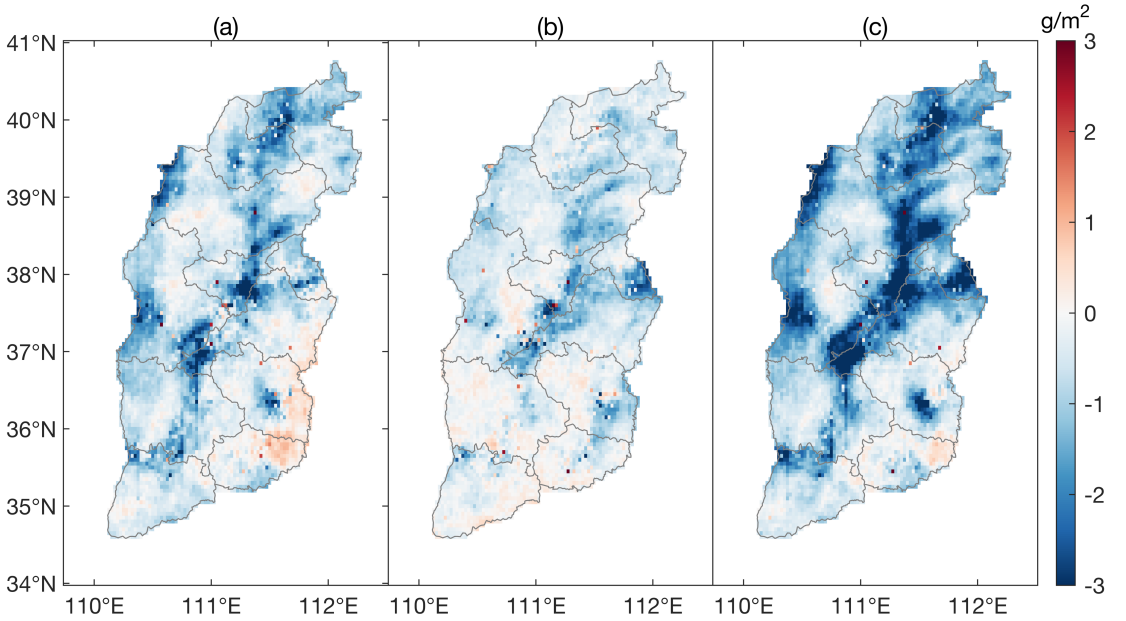

519

520 **Figure 12:** The difference between NOx emissions over Shanxi calculate based on CEMS in
521 different year: (a) Daily average mean NOx Emission of 2020 minus that of 2019; (b) Daily

522 average mean NOx Emission of 2021minus that of 2020; (c) Daily average mean NOx Emission
523 of 2021minus that of 2019.

524 3.5 Differences between Computed Emissions and a Prior Emissions Inventories

525 Three different sets of optimized emissions are calculated using MFIEF forced by
526 different a prior emissions inventories. The differences between the MFIEF emissions using
527 CEMS, MEIC050 and Merged014 are displayed in Figure 13. In general, MFIEF based on
528 MEIC050 is larger than MFIEF based on CEMS, with the major exception occurring in pixels
529 containing major polluting sources such as iron, steel, and power plants inside Taiyuan City, the
530 thermal power plants in Datong, and industrial regions in Lvliang, Jinzhong, and other cities. The
531 observed gap between the results in 2020 is even larger than in 2019, even though the overall
532 emissions in 2020 are smaller than in 2019. These differences may be due to slightly mis-
533 positioned hotspots in the existing inventory. These extreme values tend to lead to either biased
534 values of α_1 and α_2, or values which are physically impossible and therefore are discarded.
535 Furthermore, the difference between urban centers in Changzhi, Jincheng, Linfen, and Lvliang
536 may be due to the fact that CEMS better captures and detects residential sources and other
537 sources of moderate emissions, as compared with MEIC.

538 Next, the results of MFIEF based on Merged014 are usually smaller than the results of
539 MFIEF based on CEMS, with the exception of iron, steel, and power plants inside Taiyuan and
540 some other large sources where CEMS factories are located. This is because many of the grids in
541 Merged014 are so small, that when added to the original CEMS inventory, the PDF of the best fit
542 values of α_1 were shifted smaller. At the same time the values of α_2 were shifted longer. In
543 tandem with these, the transport term α_3 was shifted to include larger absolute values of
544 distance, which therefore caused the final calculation to be smaller overall. Similarly, some of
545 these shifts were so large as to make the values of α_1 and α_2 physically impossible, and
546 therefore be discarded. A similar set of shifts is observed as well when transitioning from
547 MEIC050 to MEIC014, and more so from MEIC014 to MEIC. Although mathematically correct,
548 since these shifts are not as reasonable from a physical or chemical perspective, these choices are
549 considered to be less optimal the purely relying on CEMS for the a priori value.
550

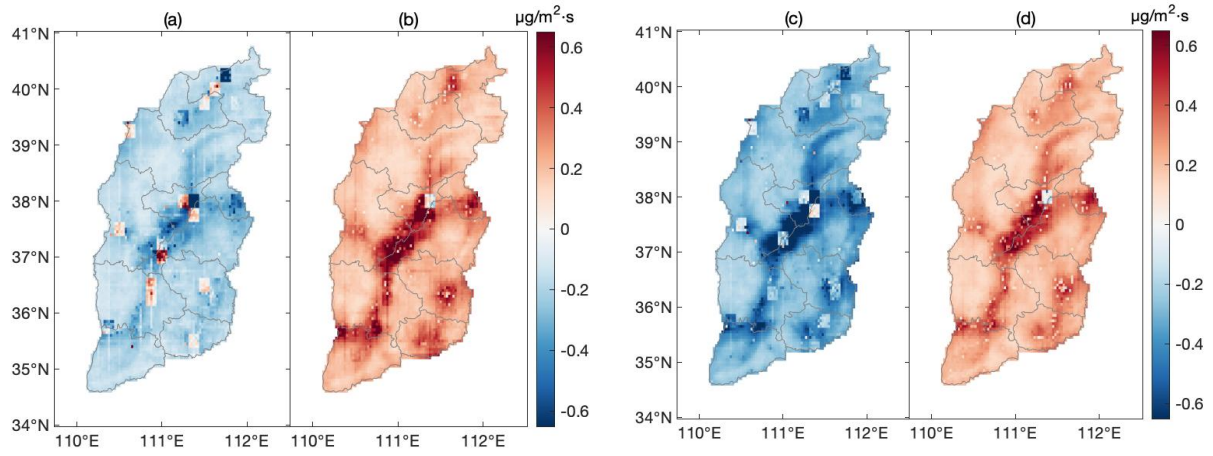

Figure 13: Computed grid-by-grid annual differences based on different a priori emissions inventories: (a) MFIEF CEMS minus MFIEF MEIC015 (February - September 2019), (b) MFIEF CEMS minus MFIEF Merged014 (February - September 2019), (c) MFIEF CEMS minus MFIEF MEIC015 (February - September 2020), (d) MFIEF CEMS minus MFIEF Merged014 (February - September 2020).

4 Conclusions

MFIEF computed emissions based on daily measurements from TROPOMI and a priori daily emissions from CEMS very successfully inverts daily NO_x emissions over a multi-year period in a rapidly developing part of China. First, the emissions computed match well with known urban, suburban, and industrial locations. Second, the best fit values for thermodynamics (α_1) and first order chemical decay (α_2) are both physically realistic, while the best fit term for transport (α_3) is reasonable based on the mountainous terrian and extensive basin-based geography of the province. Third, the computed emissions with respect to geography, month of the year, and years before and after COVID-19 are consistent with other findings from the community. Fourth, the uncertainty is observed to be lower than the day-to-day variability, showing that the results are statistically significant at the day-to-day level.

The MFIEF emissions computed using different a priori emissions datasets yield significant differences, which are not consistent with CEMS measurements or on-the-ground knowledge. The use of MEIC as an a priori severely underestimates lower and newer sources, while overestimating sources in the provincial capital of Taiyuan and its enormous steel iron plant. The MFIEF emissions computed using the mixed MEIC with CEMS a priori weights too many low values from MEIC in the suburban and rural areas, leading to physically unreasonable and very low/high biased values of α_1/α_2 values. The computed uncertainties in all of these other cases are also observed to be larger than in the base CEMS case, further indicating that these other cases are not as successful. Since MEIC is constructed similarly to EDGAR and other bottom-up emissions databases, it is possible that similar biases and results may be found in other parts of the world with respect to the geospatial biases of NO_x emissions.

The results of a variance maximization analysis of the daily TROPOMI NO_2 columns reveal three geospatial patterns that drive the NO_2 fields. This work's computed MFIEF emissions with CEMS is attributed as responsible for pattern 1, measured UV from TROPOMI (which induces photochemistry) is attributed as responsible for pattern 2, while transport

(computed from reanalysis wind and TROPOMI measured CO columns) is attributed as responsible for pattern 3. The authors recommend that subsequent emissions analysis work from both model-based and remotely-sensed based perspectives should follow a similar procedure, to ensure that the results do not only match on average, but also make sense based on the observed spatial and temporal gradients of the observed remotely sensed fields.

Finally, it is observed that the calculated values of α_1 are very highly correlated with the thermodynamic conditions of underlying large combustion sources, offering consistency that the term α_1 is a strong function of the combustion conditions under which NO_x is generated. At locations which have CEMS power plants α_1 is consistently high. At locations that have CEMS steel/iron and cement plants, α_1 is very high, but also has less consistency. Locations that have CEMS aluminum plants generally are low, but have a few individual high values of α_1. Locations that have CEMS Coke plants always have a low value of α_1, while locations with boilers consistently have the lowest α_1. There is a slight offset based on the atmospheric temperature and UV radiation, with both colder and lower radiation months having $\alpha_1$slightly negatively offset and months with hotter and higher radiation conditions having α_1 slightly positively offset. This is consistent across all plant types, but especially so for the hottest types (Iron/Steel, Cement, and Electricity), which are most likely to rise to a higher elevation and therefore be more impacted by the surrounding atmospheric conditions. These findings allow an extension of this approach to monitoring, identifying, or mode deeply understanding dedicated moderate to large emissions sources in regions which may not have surface-based monitoring.

The procedure introduced here offers a next step advance in terms of computing emissions from a top-down perspective. The authors urge the community to adopt and use these new results, while also using them to improve their own bottom-up inventories and attribution techniques. This work would be greatly improved by reduction in remotely sensed measurement errors/uncertainties, increased use of and access to surface CEMS and other flux measurements, and improved a priori emissions databases. One of the easiest ways for improvement would be for bottom-up inventories to adopt the day-to-day and other forms of variation, as well as quantitative error analyses. The ability to identify large and moderately large plants and industrial sources could be used to identify and quantify sources from many parts of the Global South where ground-based measurements may not be readily available. Finally, such objective approaches will hopefully be improved, allowing for more precision and predictability, so that emissions and environmental regulators can have more quantitative support to focus their efforts.

Acknowledgments

The authors would like to thank the continuous emissions monitoring systems (CEMS) for the provision of their in situ data. This work thanks the PIs of the TROPOMI, ERA-5, MEIC products for making their data available. The study was supported by the National Natural Science Foundation of China (42075147), the Shanxi Province Major Science and Technique Program (202101090301013), and the Shanxi Province Postgraduate Education Innovation Program (2021Y035). The authors declare that they have no conflict of interest.

Author contributions

Conceptualization: Jason Blake Cohen; Formal Analysis: Xiaolu Li, Jason Blake Cohen; Funding Acquisition: Jason Blake Cohen, Kai Qin; Investigation: Xiaolu Li, Jason Blake Cohen, Kai Qin and Hong Geng; Methodology: Xiaolu Li, Jason Blake Cohen, Kai Qin; Resources: Hong Geng, Liling Wu, Xiaohui Wu, Chengli Yang, Rui Zhang, and Liqin Zhang Software: Xiaolu Li; Supervision: Jason Blake Cohen, Kai Qin, Hong Geng; Validation: Xiaolu Li, Jason Blake Cohen; Visualization: Xiaolu Li; Writing – original draft: Xiaolu Li, Jason Blake Cohen; Writing – review & editing: Xiaolu Li, Jason Blake Cohen, Kai Qin, Hong Geng.

Data Availability Statement

The satellite NO_2 datasets used in this study are available at https://disc.gsfc.nasa.gov/datasets. The ERA-5 reanalysis product is available at https://doi.org/10.24381/cds.bd0915c6. The CEMS online data is available at https://sthjt.shanxi.gov.cn/wryjg. The MEIC product can be accessed from https://doi.org/10.6084/m9.figshare.c.5214920.v2 (Zheng et al., 2021). All of the data, including CEMS and underlying figures are available for download at https://figshare.com/s/22782c33cbc4e61afd25

References

Abyzov, A. (2019). Aluminum oxide and alumina ceramics (review). Part 1. Properties of Al_2O_3 and commercial production of dispersed Al_2O_3. *Refractories and industrial ceramics, 60*(1), 24-32. http://doi.org/10.1007/s11148-019-00304-2

Aho, M. J., Paakkinen, K. M., Pirkonen, P. M., Kilpinen, P., & Hupa, M. (1995). The effects of pressure, oxygen partial pressure, and temperature on the formation of N_2O, NO, and NO_2 from pulverized coal. *Combustion and Flame, 102*(3), 387-400. https://doi.org/10.1016/0010-2180(95)00019-3

Akgun, F. (2003). Investigaton of energy saving and NO_x reduction possibilities in a rotary cement kiln. *International journal of energy research, 27*(4), 455-465. https://doi.org/10.1002/er.888

Beirle, S., Boersma, K. F., Platt, U., Lawrence, M. G., & Wagner, T. (2011). Megacity Emissions and Lifetimes of Nitrogen Oxides Probed from Space. *Science, 333*(6050), 1737-1739. https://doi.org/10.1126/science.1207824

Beirle, S., Borger, C., Dorner, S., Li, A., Hu, Z. K., Liu, F., et al. (2019). Pinpointing nitrogen oxide emissions from space. *Science Advances, 5*(11). https://www.science.org/doi/10.1126/sciadv.aax9800

Björnsson, H., & Venegas, S. (1997). A manual for EOF and SVD analyses of climatic data. *CCGCR Report, 97*(1), 112-134. McGill University.

Bond, T. C. (2004). A technology-based global inventory of black and organic carbon emissions from combustion. *Journal of Geophysical Research, 109*(D14). https://doi.org/10.1029/2003JD003697

Chen, Y. H., & Prinn, R. G. (2006). Estimation of atmospheric methane emissions between 1996 and 2001 using a three-dimensional global chemical transport model. *Journal of Geophysical Research: Atmospheres, 111*(D10). https://doi.org/10.1029/2005JD006058

Cohen, J. B. (2014). Quantifying the occurrence and magnitude of the Southeast Asian fire climatology. *Environmental Research Letters, 9*(11). https://doi.org/10.1088/1748-9326/9/11/114018

Cohen, J. B., Lecoeur, E., & Hui Loong Ng, D. (2017). Decadal-scale relationship between measurements of aerosols, land-use change, and fire over Southeast Asia. *Atmospheric Chemistry and Physics, 17*(1), 721-743. https://doi.org/10.5194/acp-17-721-2017

Cohen, J. B., Ng, D. H. L., Lim, A. W. L., & Chua, X. R. (2018). Vertical distribution of aerosols over the Maritime Continent during El Nino. *Atmospheric Chemistry and Physics, 18*(10), 7095-7108. https://doi.org/18/7095/2018/acp-18-7095-2018

Cohen, J. B., & Wang, C. (2014). Estimating global black carbon emissions using a top-down Kalman Filter approach. *Journal of Geophysical Research-Atmospheres, 119*(1), 307-323. https://doi.org/10.1002/2013jd019912

Crippa, M., Guizzardi, D., Muntean, M., Schaaf, E., Dentener, F., van Aardenne, J. A., et al. (2018). Gridded emissions of air pollutants for the period 1970–2012 within EDGAR v4.3.2. *Earth System Science Data, 10*(4), 1987-2013. https://doi.org/10.5194/essd-10-1987-2018

Eskes, H., Geffen, J. v., Boersma,F., Eichmann, K.-U., Apituley, A., Pedergnana, M., et al. (2021). *Sentinel-5 precursor/TROPOMI Level 2 Product User Manual Nitrogendioxide*. Royal Netherlands Meteorological Institute.

Fioletov, V., McLinden, C. A., Griffin, D., Krotkov, N., Liu, F., & Eskes, H. (2022). Quantifying urban, industrial, and background changes in NO_2 during the COVID-19 lockdown period based on TROPOMI satellite observations. *Atmospheric Chemistry and Physics, 22*(6), 4201-4236. https://doi.org/10.5194/acp-22-4201-2022

Geng, G., Xiao, Q., Zheng, Y., Tong, D., Zhang, Y., Zhang, X., et al. (2019). Impact of China's air pollution prevention and control action plan on $PM_{2.5}$ chemical composition over

688 eastern China. *Science China Earth Sciences, 62*(12), 1872-1884.
689 https://doi.org/10.1007/s11430-018-9353-x
690 Goldberg, D. L., Lu, Z., Streets, D. G., de Foy, B., Griffin, D., McLinden, C. A., et al. (2019).
691 Enhanced capabilities of TROPOMI NO_2: estimating NO_x from North American Cities
692 and power plants. *Environmental Science & Technology, 53*(21), 12594-12601.
693 https://doi.org/10.1021/acs.est.9b04488
694 Griffin, D., McLinden, C. A., Boersma, F., Bourassa, A., Dammers, E., Degenstein, D., et al.
695 (2019). High resolution mapping of nitrogen dioxide with TROPOMI: First results and
696 validation over the Canadian oil sands. *Geophysical Research Letters, 46*(2), 1049-1060.
697 https://doi.org/10.1029/2018GL081095
698 Hoesly, R. M., Smith, S. J., Feng, L., Klimont, Z., Janssens-Maenhout, G., Pitkanen, T., et al.
699 (2018). Historical (1750-2014) anthropogenic emissions of reactive gases and aerosols
700 from the Community Emissions Data System (CEDS). *Geoscientific Model Development,*
701 *11*(1), 369-408. https://doi.org/10.5194/gmd-11-369-2018
702 Hu, Y., Zang, Z., Chen, D., Ma, X., Liang, Y., You, W., et al. (2022). Optimization and
703 evaluation of SO_2 emissions based on WRF-Chem and 3DVAR data assimilation, *Remote*
704 *Sensing*, *14*(1), 220. https://doi.org/10.3390/rs14010220
705 Jacob, D. J., Logan, J. A., Gardner, G. M., Yevich, R. M., Spivakovsky, C. M., Wofsy, S. C., et
706 al. (1993). Factors regulating ozone over the United States and its export to the global
707 atmosphere. *Journal of Geophysical Research: Atmospheres, 98*(D8), 14817-14826.
708 https://doi.org/10.1029/98JD01224
709 Jiang, X., Li, G., & Fu, W. (2021). Government environmental governance, structural adjustment
710 and air quality: A quasi-natural experiment based on the Three-year Action Plan to Win
711 the Blue Sky Defense War. *Journal of Environmental Management, 277*, 111470.
712 https://doi.org/10.1029/2018GL081095
713 Karplus, V. J., Zhang, S., & Almond, D. (2018). Quantifying coal power plant responses to
714 tighter SO2 emissions standards in China. *Proc Natl Acad Sci U S A, 115*(27), 7004-
715 7009. https://doi.org/10.1073/pnas.1800605115
716 Kong, H., Lin, J., Zhang, R., Liu, M., Weng, H., Ni, R., et al. (2019). High-resolution
717 ($0.05° \times 0.05°$) NO_x emissions in the Yangtze River Delta inferred from OMI.

718 *Atmospheric Chemistry and Physics, 19*(20), 12835-12856.
719 https://doi.org/10.5194/acp19-12835-2019
720 Lange, K., Richter, A., & Burrows, J. P. (2022). Variability of nitrogen oxide emission fluxes
721 and lifetimes estimated from Sentinel-5P TROPOMI observations. *Atmospheric*
722 *Chemistry and Physics, 22*(4), 2745-2767. https://doi.org/10.5194/acp-22-2745-2022
723 Le Bris, T., Cadavid, F., Caillat, S., Pietrzyk, S., Blondin, J., & Baudoin, B. (2007). Coal
724 combustion modelling of large power plant, for NO_x abatement. *Fuel, 86*(14), 2213-2220.
725 https://doi.org/10.1016/j.fuel.2007.05.054
726 Li, H., Zhang, J., Wen, B., Huang, S., Gao, S., Li, H., et al. (2022). Spatial-Temporal
727 Distribution and Variation of NO2 and Its Sources and Chemical Sinks in Shanxi
728 Province, China. *Atmosphere, 13*(7), 1096. https://doi.org/10.3390/atmos13071096
729 Lin, C., Cohen, J. B., Wang, S., & Lan, R. (2020). Application of a combined standard deviation
730 and mean based approach to MOPITT CO column data, and resulting improved
731 representation of biomass burning and urban air pollution sources. *Remote Sensing of*
732 *Environment, 241*, 111720. https://doi.org/10.1016/j.rse.2020.111720
733 Liu, J., & Cohen, J. (2022). Quantifying the Missing Half of Daily NO_x Emissions over South,
734 Southeast and East Asia. https://doi.org/10.21203/rs.3.rs-1613262/v1
735 Mahowald, N. M., Baker, A. R., Bergametti, G., Brooks, N., Duce, R. A., Jickells, T. D., et al.
736 (2005). Atmospheric global dust cycle and iron inputs to the ocean. *Global*
737 *Biogeochemical Cycles, 19*(4). https://doi.org/10.1029/2004gb002402
738 Mijling, B., & van der A, R. J. (2012). Using daily satellite observations to estimate emissions of
739 short-lived air pollutants on a mesoscopic scale. *Journal of Geophysical Research:*
740 *Atmospheres, 117*(D17). https://doi.org/10.1029/2012JD017817.
741 Neto, G. F., Leite, M., Marcelino, T., Carneiro, L., Brito, K., & Brito, R. (2021). Optimizing the
742 coke oven process by adjusting the temperature of the combustion chambers. *Energy,*
743 *217*, 119419. https://doi.org/10.1016/j.energy.2020.119419
744 Qin, K., Shi, J., He, Q., Deng, W., Wang, S., Liu, J., & Cohen, J. B. (2022). New Model-Free
745 Daily Inversion of NO_x Emissions using TROPOMI (MCMFE-NO_x): Deducing a See-
746 Saw of Halved Well Regulated Sources and Doubled New Sources. *Earth and Space*
747 *Science Open Archive*, 26. https://doi.org/10.1002/essoar.10512010.1

748 Schreifels, J. J., Fu, Y. L., & Wilson, E. J. (2012). Sulfur dioxide control in China: policy
749 evolution during the 10th and 11th Five-year Plans and lessons for the future. *Energy*
750 *Policy, 48*, 779-789. https://doi.org/10.1016/j.enpol.2012.06.015
751 Schwerdt, C. (2006). *Modelling NO_x-formation in combustion processes*. *Master Theses*. Lund
752 University
753 Shanxi DEE. (2016, 2021). *Shanxi Province Ecology and Environment Status Bulletin*.
754 Department of Ecology and Environment of Shanxi Province.
755 https://sthjt.shanxi.gov.cn/zwgk/hjgb/hjzkgb/index.shtml
756 Singh, A., & Agrawal, M. (2008). Acid rain and its ecological consequences. *Journal of*
757 *Environmental Biology, 29*(1), 15-24.
758 Tang, L., Xue, X., Qu, J., Mi, Z., Bo, X., Chang, X., et al. (2020). Air pollution emissions from
759 Chinese power plants based on the continuous emission monitoring systems network. *Sci*
760 *Data, 7*(1), 325. https://doi.org/10.1038/s41597-020-00665-1
761 Tu, Q., Hase, F., Schneider, M., García, O., Blumenstock, T., Borsdorff, T., et al. (2022).
762 Quantification of CH_4 emissions from waste disposal sites near the city of Madrid using
763 ground- and space-based observations of COCCON, TROPOMI and IASI. *Atmospheric*
764 *Chemistry and Physics, 22*(1), 295-317. https://doi.org/10.5194/acp-22-295-2022
765 Tu, Q., Schneider, M., Hase, F., Khosrawi, F., Ertl, B., Necki, J., et al. (2022). Quantifying CH_4
766 emissions in hard coal mines from TROPOMI and IASI observations using the wind-
767 assigned anomaly method. *Atmospheric Chemistry and Physics, 22*(15), 9747-9765.
768 https://doi.org/10.5194/acp-22-9747-2022
769 Turns, S. R. (1995). Understanding NO_x formation in nonpremixed flames: Experiments and
770 modeling. *Progress in Energy and Combustion Science, 21*(5), 361-385.
771 https://doi.org/10.1016/0360-1285(94)00006-9
772 Valin, L. C., Russell, A. R., & Cohen, R. C. (2013). Variations of OH radical in an urban plume
773 inferred from NO2 column measurements. *Geophysical Research Letters, 40*(9), 1856-
774 1860. https://doi.org/10.1002/grl.50267
775 Veefkind, J. P., Aben, I., McMullan, K., Förster, H., de Vries, J., Otter, G., et al. (2012).
776 TROPOMI on the ESA Sentinel-5 Precursor: A GMES mission for global observations of
777 the atmospheric composition for climate, air quality and ozone layer applications. *Remote*
778 *Sensing of Environment, 120*, 70-83. https://doi.org/10.1016/j.rse.2011.09.027

779 Wang, H., Rasch, P. J., Easter, R. C., Singh, B., Zhang, R., Ma, P. L., et al. (2014). Using an
780 explicit emission tagging method in global modeling of source-receptor relationships for
781 black carbon in the Arctic: Variations, sources, and transport pathways. *Journal of*
782 *Geophysical Research: Atmospheres, 119*(22). https://doi.org/10.1002/2014jd022297
783 Wang, S., Cohen, J. B., Deng, W., Qin, K., & Guo, J. (2021). Using a New Top-Down
784 Constrained Emissions Inventory to Attribute the Previously Unknown Source of
785 Extreme Aerosol Loadings Observed Annually in the Monsoon Asia Free Troposphere.
786 *Earth's Future, 9*(7). https://doi.org/10.1029/2021ef002167
787 Wang, S., Cohen, J. B., Lin, C. Y., & Deng, W. Z. (2020). Constraining the relationships
788 between aerosol height, aerosol optical depth and total column trace gas measurements
789 using remote sensing and models. *Atmospheric Chemistry and Physics, 20*(23), 15401-
790 15426. https://doi.org/10.5194/acp-20-15401-2020
791 Wu, H., Cai, J., Ren, Q., Shi, C., Zhao, A., & Lyu, Q. (2020). A thermal and chemical fuel
792 pretreatment process for NO_x reduction from cement kiln. *Fuel Processing Technology,*
793 *210*, 106556. https://doi.org/10.1016/j.fuproc.2020.106556
794 Zavala, M., Herndon, S. C., Slott, R. S., Dunlea, E. J., Marr, L. C., Shorter, J. H., et al. (2006).
795 Characterization of on-road vehicle emissions in the Mexico City Metropolitan Area
796 using a mobile laboratory in chase and fleet average measurement modes during the
797 MCMA-2003 field campaign. *Atmospheric Chemistry and Physics, 6*(12), 5129-5142.
798 https://doi.org/10.5194/acp-6-5129-2006
799 Zhang, X., & Schreifels, J. (2011). Continuous emission monitoring systems at power plants in
800 China: Improving SO_2 emission measurement. *Energy Policy, 39*(11), 7432-7438.
801 https://doi.org/10.1016/j.enpol.2011.09.011
802 Zhang, Z., Zang, Z., Cheng, X., Lu, C., Huang, S., Hu, Y., et al. (2021). Development of three-
803 dimensional variational data assimilation method of aerosol for the CMAQ model: an
804 application for $PM_{2.5}$ and PM_{10} forecasts in the sichuan basin. *Earth and Space Science,*
805 *8*(5), e2020EA001614. https://doi.org/10.1029/2020EA001614
806 Zhao, Y., Nielsen, C. P., Lei, Y., McElroy, M. B., & Hao, J. (2011). Quantifying the
807 uncertainties of a bottom-up emission inventory of anthropogenic atmospheric pollutants
808 in China. *Atmospheric Chemistry and Physics, 11*(5), 2295-2308.
809 https://doi.org/10.5194/acp-11-2295-2011

Zheng, B., Zhang, Q., Geng, G., Chen, C., Shi, Q., Cui, M., et al. (2021). Changes in China's anthropogenic emissions and air quality during the COVID-19 pandemic in 2020. *Earth System Science Data, 13*(6), 2895-2907. https://doi.org/10.5194/essd-13-2895-2021

Zheng, B., Zhang, Q., Tong, D., Chen, C., Hong, C., Li, M., et al. (2017). Resolution dependence of uncertainties in gridded emission inventories: a case study in Hebei, China. *Atmospheric Chemistry and Physics, 17*(2), 921-933. https://doi.org/10.5194/acp-17-921-2017

Zhou, H., Ma, P., Cheng, M., Zhou, M., & Li, Y. (2018). Effects of temperature and circulating flue gas components on combustion and NO_x emissions characteristics of four types quasi-particles in iron ore sintering process. *ISIJ International, 58*(9), 1650-1658. https://doi.org/10.2355/isijinternational.ISIJINT-2018-185

Zhou, S., Davy, P. K., Wang, X., Cohen, J. B., Liang, J., Huang, M., et al. (2016). High time-resolved elemental components in fine and coarse particles in the Pearl River Delta region of Southern China: Dynamic variations and effects of meteorology. *The Science of the total environment*, *572*, 634-648. https://doi.org/10.1016/j.scitotenv.2016.05.194